

Emergent Dirac carriers across a pressure-induced Lifshitz transition in black phosphorusP. Di Pietro,¹ M. Mitrano,² S. Caramazza,³ F. Capitani,^{3,4} S. Lupi,⁵ P. Postorino,⁵ F. Ripanti,³ B. Joseph,³ N. Ehlen,⁶ A. Grüneis,⁶ A. Sanna,⁷ G. Profeta,⁸ P. Dore,⁹ and A. Perucchi^{1,*}¹*Elettra-Sincrotrone Trieste, Area Science Park, I-34012 Trieste, Italy*²*Department of Physics and Materials Research Laboratory, University of Illinois at Urbana-Champaign, Illinois 61801, USA*³*Dipartimento di Fisica, Università di Roma Sapienza, Piazzale Aldo Moro 2, I-00185 Roma, Italy*⁴*Synchrotron SOLEIL, L'Orme des Merisiers, Saint-Aubin, 91192 Gif-sur-Yvette, France*⁵*CNR-IOM and Dipartimento di Fisica, Università di Roma Sapienza, Piazzale Aldo Moro 2, I-00185 Roma, Italy*⁶*Physikalishes Institut, Universität zu Köln, Zùlpicher Strasse 77, 50937 Köln, Germany*⁷*Max Planck Institut für Mikrostrukturphysik, Weinberg 2, D-06120 Halle, Germany*⁸*CNR-SPIN and Dipartimento di Fisica, Università degli Studi di L'Aquila, Via Vetoio 10, I-67100 L'Aquila, Italy*⁹*CNR-SPIN and Dipartimento di Fisica, Università di Roma Sapienza, Piazzale Aldo Moro 2, I-00185 Roma, Italy*

(Received 19 April 2018; published 8 October 2018)

The phase diagram of correlated systems like cuprate or pnictide high-temperature superconductors is likely defined by a topological change of the Fermi surface under continuous variation of an external parameter, the so-called Lifshitz transition. However, a number of low-temperature instabilities and the interplay of multiple energy scales complicate the study of this phenomenon. Here we identify the optical signatures of a pressure-induced Lifshitz transition in a clean elemental system, black phosphorus. By applying external pressures above 1.5 GPa, we observe a change in the pressure-dependent Drude plasma frequency due to the appearance of massless Dirac fermions. At higher pressures, optical signatures of two structural phase transitions are also identified. Our findings suggest that a key fingerprint of the Lifshitz transition, in the absence of structural transitions, is a Drude plasma frequency discontinuity due to a change in the Fermi surface topology.

DOI: [10.1103/PhysRevB.98.165111](https://doi.org/10.1103/PhysRevB.98.165111)**I. INTRODUCTION**

The Lifshitz transition, the change of the Fermi surface topology under variation of an external parameter [1], is suspected to play a relevant role in determining the electronic properties of strongly correlated systems like the $\text{YBa}_2\text{Cu}_3\text{O}_{6+y}$ [2], $\text{Bi}_2\text{Sr}_2\text{CaCu}_2\text{O}_{8+\delta}$ [3], and $\text{Ba}(\text{Fe}_{1-x}\text{Co}_x)_2\text{As}_2$ [4] superconductors. In these materials, it may induce a band flattening and increase the density of states close to the Fermi level, thus promoting the onset of high-temperature superconductivity [5]. However, these compounds also exhibit additional low-temperature phase transitions that can mask the thermodynamic and transport properties of a pure Lifshitz transition. As a result, the dynamical charge and current fluctuations across a Lifshitz transition are still poorly understood.

Several Lifshitz transitions have been observed (or theoretically predicted) in elemental black phosphorus (BP), as a function of doping [6,7], electric field [8], and pressure [9,10]. BP is an attractive material for electronic applications due to its very high electron mobility ($10^4 \text{ cm}^2\text{V}^{-1}\text{s}^{-1}$) and the presence of a direct, tunable infrared band gap [11]. Its A17 orthorhombic structure is extremely anisotropic, with grooves oriented along the so-called zigzag direction [12] [see Fig. 1(a)]. The band structure is parabolic along both the interlayer and the zigzag directions, while along the armchair direction the dispersion is almost linear, thus allowing possible

Dirac cones [13,14]. Upon pressurization, both the structure and the electronic properties undergo dramatic changes and a Lifshitz transition occurs at a pressure $P_L = 1.5 \text{ GPa}$ [see Fig. 1(b)]. At low pressures, the electronic band gap gradually closes until the valence and conduction bands touch at the Z point, before intersecting each other without hybridizing. Around P_L , four-fold degenerate Dirac points are formed, which are then evolving in both electronlike and holelike Fermi pockets when the pressure is further increased [15]. At $P > P_L$, the orthorhombic (A17) structure becomes rhombohedral (A7) around 5 GPa and then simple cubic (sc) around 10 GPa [16–19], where superconductivity also occurs [20,21].

The occurrence of a pressure-induced Lifshitz transition in an elemental semiconductor provides a unique setting for the study of its electrostatics in the absence of other low-temperature instabilities. Here, we address this topic by driving BP across the pressure-induced Lifshitz transition and studying its optical response with synchrotron-based infrared spectroscopy and first principles density functional theory (DFT) calculations. We identify the optical signatures of a pressure-induced topological Lifshitz transition in an elemental semiconductor. At a transition pressure $P_L = 1.5 \text{ GPa}$, BP evolves from a semiconductor to a Dirac semimetal by building up a plasma of massless charge carriers. At higher pressures, we observe the optical fingerprints of the two structural phase transitions occurring in the semimetal phase.

II. EXPERIMENT

Our infrared measurements under pressure were performed at the SISSI infrared beamline [22] of the Elettra storage

*andrea.perucchi@elettra.eu

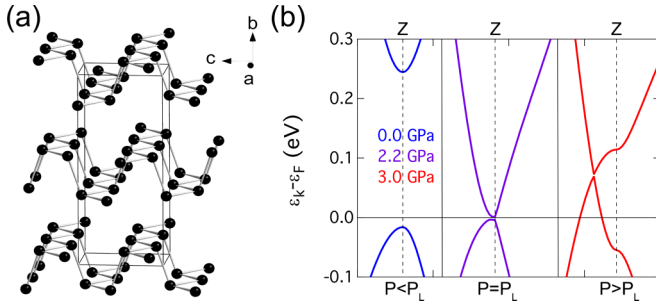


FIG. 1. (a) Crystallographic unit cell of BP. (b) Valence and conduction bands of BP at the Z point (marked by a dashed line) across the pressure-induced Lifshitz transition. P_L is the Lifshitz transition pressure, while the Z points are offset in momentum for clarity.

ring, with a Bruker 70v interferometer mated to a broadband infrared microscope. BP samples were obtained from two different providers (Smart-Elements and HQ Graphene) and cut for use in a diamond anvil cell (DAC) with CsI as the pressure transmitting medium, yielding identical experimental results. The samples, oriented along the basal ac plane [see Fig. 1(a)], were kept in contact with the diamonds in order to ensure a flat interface. Pressure was gauged through the ruby fluorescence technique [23]. The samples were mounted in two different DACs equipped with 1.0 and 0.4 mm culet diamonds respectively. The former allowed reliable measurements down to 100 cm^{-1} for pressures up to 2.2 GPa, while the latter allowed up to 10.4 GPa. Light was polarized along the most conductive direction, the c (armchair) axis crystallographic direction. From the reflectivity data at the sample-diamond interface we retrieved the optical conductivity through Kramers-Kronig transformations [24,25]. All the measurements reported in this study were performed at room temperature (RT).

III. ELECTRODYNAMICS OF THE LIFSHITZ TRANSITION

We report in Fig. 2 the infrared signatures of the pressure-induced Lifshitz transition in the orthorhombic phase of BP, the key experimental observation of this work. Above 200 cm^{-1} , the low-pressure ($< 1.0 \text{ GPa}$) reflectivity $R(\omega)$ is approximately 0.1, and remains flat in the whole measured range, up to 8000 cm^{-1} . The real part of the optical conductivity $\sigma_1(\omega)$ is very low and consistent with semiconducting behavior at ambient pressure. As pressure is increased, both $R(\omega)$ and $\sigma_1(\omega)$ are gradually enhanced. However, between 1.3 and 1.6 GPa we observe an abrupt blueshift of the reflectivity plasma edge that can be ascribed to the Lifshitz transition observed in angle-resolved photoemission spectroscopy (ARPES) [6]. As pressure is further increased and the phonon becomes screened, a Drude-like absorption term appears due to the delocalization of charge carriers.

A reliable, model-independent figure of merit for the pressure-induced metallization is the low-frequency spectral weight [24], $\text{SW} = \frac{120}{\pi} \int_{\Omega_1}^{\Omega_2} \sigma(\omega) d\omega$, integrated between $\Omega_1 = 100 \text{ cm}^{-1}$ and $\Omega_2 = 200 \text{ cm}^{-1}$. Ω_1 is the low-frequency limit of our data, while Ω_2 is chosen in order to fully include the low-frequency Drude term. As is visible in Fig. 2(c), the

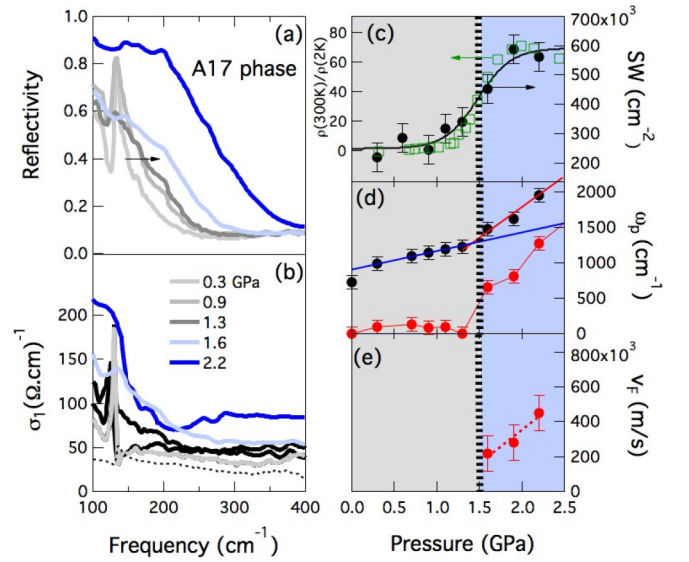


FIG. 2. Optical reflectivity at the sample-diamond interface (a) and real part of the optical conductivity (b) of orthorhombic BP measured along the c -axis polarization direction. The ambient pressure optical conductivity is also reported for comparison as a black dashed line. (c) Spectral weight (SW) of $\sigma_1(\omega)$ integrated between 100 and 200 cm^{-1} . SW follows a phenomenological sigmoid behavior centered at $P_L = 1.5 \text{ GPa}$ (dashed vertical line). The resistivity ratio $\rho(300 \text{ K})/\rho(2 \text{ K})$ from Ref. [9] is also reported for comparison. (d) Plasma frequency ω_p (from Lorentz-Drude fitting) vs pressure. Black circles represent the bare ω_p , while red circles mark the Dirac ω_p (see text). (e) Fermi velocity of Dirac carriers from Eq. (1). The red dashed line is a guide to the eye.

pressure dependent SW follows a sigmoid trend centered at $P_L = 1.5 \text{ GPa}$. This behavior maps exactly onto the resistivity measurement from Ref. [9] [see Fig. 2(c)], and was previously associated with the Lifshitz transition.

In order to quantify the carrier density changes across the transition, we performed Drude-Lorentz fits to the data (see the Appendix). The plasma frequency (ω_p) associated with the free-carrier Drude term is reported in Fig. 2(d) as a function of pressure. It is worth noting that a small, but notable RT conductivity in the order of a few tens $(\Omega \text{ cm})^{-1}$ is observed also at ambient pressure, i.e., in the semiconducting phase, and can be ascribed to the presence of thermally activated carriers. Notably, the plasma frequency increases linearly with pressure, up to P_L .

At the Lifshitz transition pressure P_L , ω_p increases more steeply at a rate of $900 \text{ cm}^{-1}/\text{GPa}$, almost three times the $260 \text{ cm}^{-1}/\text{GPa}$ slope observed below P_L . The discontinuity in the plasma frequency slopes can be ascribed to the simultaneous presence of different fermions contributing to the conduction. Below P_L only massive, thermally activated carriers contribute to the conduction. As the Dirac cone is formed above P_L , also Dirac-like fermions contribute to the Drude conductivity, thus leading to a combination of massive (Schrödinger-like) and massless (Dirac) carriers. We evaluate the massive carrier contribution ($\omega_{p,s}$) at all pressures by extrapolating above P_L the linear behavior of ω_p from below P_L . As a consequence, the massless Dirac contribution to the

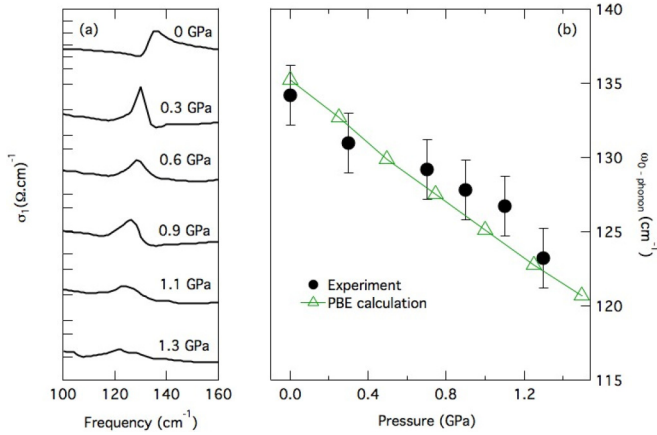


FIG. 3. (a) Detail of the B_{1u} phonon mode for selected pressures. (b) Pressure-dependent B_{1u} phonon frequency from experimental data and *ab initio* calculations described in Sec. V.

plasma frequency $\omega_{p,D}$ can be calculated at all pressures from $\omega_p^2 = \omega_{p,S}^2 + \omega_{p,D}^2$. The resulting pressure dependent $\omega_{p,D}$ is reported in Fig. 2(d).

The massless Dirac plasma frequency $\omega_{p,D}$ can be microscopically calculated as [26]

$$\omega_{p,D} = \sqrt{\frac{e^2}{\hbar v_F} \left(\frac{32\pi g_s g_v}{3} \right)^{1/6} n^{1/3} v_F}, \quad (1)$$

where g_s and g_v are the spin and valley degeneracies ($g_s = 2$ and $g_v = 2$ in BP [27]). By making use of the experimental density of carriers determined from Hall effect measurements [28], we can use Eq. (1) to estimate the pressure-dependent Fermi velocity v_F [reported in Fig. 4(c)], and we find it to be around $(2-4) \times 10^5$ m/s, in good agreement with theoretical calculations [15].

Within the A17 phase, we also detect a sharp peak at 130 cm^{-1} that is assigned to the B_{1u} phonon mode [29] [see Figs. 2(a)–2(b)]. The pressure dependent behavior of this vibrational feature is reported in Fig. 3(a). The B_{1u} phonon displays a quite pronounced asymmetric (Fano) behavior, thus indicating the interaction with a higher-frequency continuum. As pressure increases, the phonon becomes screened and less asymmetric while a Drude-like absorption term centered at zero frequency appears to be due to charge carrier delocalization. Its center frequency continuously redshifts from 134 to 123 cm^{-1} at 1.3 GPa , as shown in Fig. 3(b). At higher pressures, the phonon is completely screened in the optical conductivity and cannot be followed further. The pressure dependent behavior is well captured by *ab initio* calculations described in Sec. V.

IV. INFRARED PROPERTIES IN THE A7 AND SIMPLE CUBIC PHASES

By further increasing pressure well above P_L , BP undergoes two distinct structural phase transitions: from orthorhombic (A17) to rhombohedral (A7) and from rhombohedral to simple cubic (sc), at about 5 and 10 GPa respectively [16,17,20]. Recent experiments hint at the presence of large regions of phase coexistence between the various structural

phases [30–33]. According to x-ray diffraction data from Ref. [32], performed on the same batch of samples used in this work, the A7 phase starts to appear above 5 GPa and coexists with A17 up to 10 GPa . Above this pressure, the A7 phase disappears, while the sc phase gradually sets in.

We report in Figs. 4(a) and 4(b) the optical properties across the A17-A7 phase transition to investigate how the mixed Drude term responds to a structural phase transition. Under increasing pressure, the infrared reflectivity is enhanced and its plasma edge monotonically blueshifts [see Fig. 4(e)], while the optical conductivity increases. The optical gap, located roughly at $\sim 2000 \text{ cm}^{-1}$ [see the ambient pressure $\sigma_1(\omega)$ reported in Fig. 4(b) for reference] is filled up. In this pressure range, the optical conductivity can be described by the combination of a Drude term and a midinfrared (MIR) band (see the Appendix). The Drude plasma frequency grows linearly with pressure [black circles in Fig. 4(e)] with the same $900 \text{ cm}^{-1}/\text{GPa}$ slope observed at 1.5 GPa . With increasing pressure, the MIR band progressively coalesces into the Drude and becomes a second zero-frequency oscillator with a scattering rate $\gamma \sim 6000 \text{ cm}^{-1}$, i.e., much larger than the one associated with the massless carriers ($\gamma \sim 50-500 \text{ cm}^{-1}$). Remarkably, when summed in quadrature ($\omega_{p,\text{Drude}+\text{MIR}}$), the two Drude terms exhibit a linear increase with the same slope of $900 \text{ cm}^{-1}/\text{GPa}$ discussed above [see Fig. 4(e)]. In this pressure range the decomposition of ω_p in terms of $\omega_{p,D}$ and $\omega_{p,S}$ becomes relatively unimportant because of the dominance of the $\omega_{p,D}$ contribution [see Fig. 4(e)].

When entering the high-pressure A7-sc mixed phase, the optical properties drastically change [Figs. 4(c) and 4(d)]. The reflectivity edge shifts to 8000 cm^{-1} , resulting in a greatly enhanced $\sigma_1(\omega)$. The two-band electronic structure clearly identified in the A17-A7 mixed phase appears now to be merged into one single Drude term (see the Appendix) with $\omega_p \sim 15000 \text{ cm}^{-1}$, roughly corresponding to the $\omega_{p,\text{Drude}+\text{MIR}}$ term introduced before to describe the A17-A7 phase.

V. THEORETICAL BAND STRUCTURE CALCULATIONS

Our experimental findings can be benchmarked against first-principles density functional theory (DFT) calculations of the structural, electronic, and optical properties under pressure. A first-principles description of the BP electronic properties across the semiconductor-metal transition is challenging for local DFT exchange-correlation functionals, which predict a metallic ground state at ambient conditions. In order to reproduce the small band gap at ambient conditions, we used the Tran-Blaha [34] meta-GGA exchange-correlation potential in DFT calculations [35], which is quite reliable for describing small-gap *sp* systems. The calculated zero-pressure band gap is 2000 cm^{-1} for the experimental, ambient-pressure lattice parameters, in agreement with the ambient pressure optical conductivity [see Fig. 3(b)], and previous experimental reports [6,14].

Experimental lattice constants [17] and internal phosphorus positions as a function of pressure have been used to determine the electronic and optical properties as well [see calculated pressure-dependent band structures in Fig. 5]. The optical properties, plasma frequency tensor, and frequency-dependent real and imaginary dielectric matrix have been

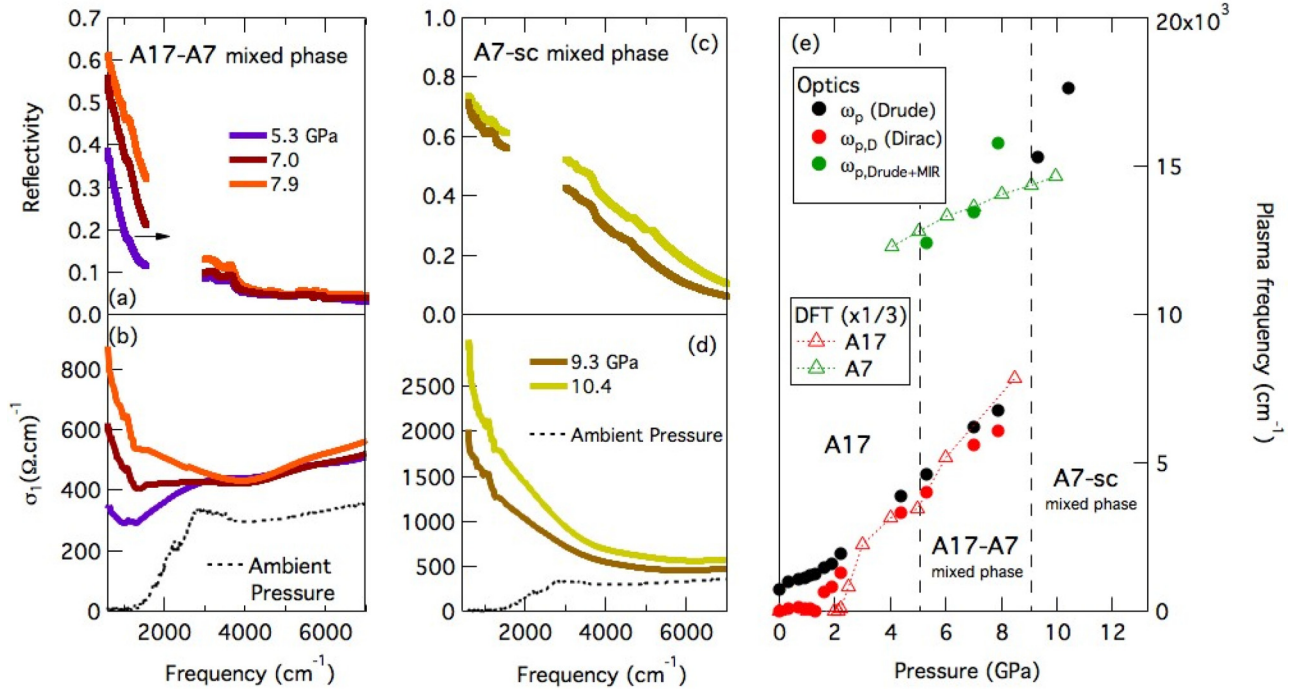


FIG. 4. Optical reflectivity at the sample-diamond interface (a) and real optical conductivity (b) of BP measured along the c -axis polarization direction in the A17-A7 mixed phase. (c)-(d) Same quantities in the A7-sc mixed phase. The ambient pressure optical conductivity is reported for comparison as a dashed line in panels (b) and (d). (e) Experimental (full circles) and theoretical (empty triangles) Drude plasma frequencies across the structural phase transitions. Black circles represent the bare Drude-Lorentz plasma frequency. The Dirac plasma frequency (red circles) is obtained by subtracting the plasma frequency of the thermally activated massive carriers. The sum in quadrature of the Drude and MIR band plasma frequencies is shown as green circles. Red and green triangles are the rescaled DFT plasma frequencies in the A17 and A7 phases, respectively.

calculated from the band structure, including the interband transitions without local-field effects [36]. The optical conductivity tensor $\sigma(\omega)$ is related to the dielectric function by (atomic units are used throughout)

$$\epsilon_{\alpha\beta}(\omega) = \delta_{\alpha\beta} + \frac{4\pi i}{\omega} \sigma_{\alpha\beta}(\omega), \quad (2)$$

for Cartesian components α, β , and $\sigma_{\alpha\beta}(\omega)$ is

$$\begin{aligned} \sigma_{\alpha\beta}(\omega) = & -\frac{i}{\Omega} \sum_{v\mathbf{k}} \frac{w_{\mathbf{k}}}{\epsilon_{v\mathbf{k}}} \left[\frac{\Pi_{vc}^{\alpha}(\mathbf{k})\Pi_{cv}^{\beta}(\mathbf{k})}{\omega + \epsilon_{v\mathbf{k}} + i\eta} + \frac{(\Pi_{vc}^{\alpha}(\mathbf{k})\Pi_{cv}^{\beta}(\mathbf{k}))^*}{\omega - \epsilon_{v\mathbf{k}} + i\eta} \right] \\ & + \frac{i(\omega_p)_{\alpha\beta}}{4\pi} \frac{1}{\omega + i\eta}, \end{aligned} \quad (3)$$

where the first and second terms are the interband and the intraband contributions respectively and η is a positive infinitesimal constant; $\epsilon_{v\mathbf{k}} \equiv \epsilon_{v\mathbf{k}} - \epsilon_{c\mathbf{k}}$ are the differences between valence and conduction eigenvalues; $w_{\mathbf{k}}$ are k -point weights over the Brillouin zone; Ω is the unit cell volume; and

$$\Pi_{vc}(\mathbf{k}) \equiv \langle v\mathbf{k} | \hat{p} | c\mathbf{k} \rangle \quad (4)$$

are the momentum matrix elements. The plasma frequency is given by

$$(\omega_p^2)_{\alpha\beta} = \frac{4\pi}{\Omega} \sum_{n\mathbf{k}} w_{\mathbf{k}} \Pi_{nn}^{\alpha}(\mathbf{k}) \Pi_{nn}^{\beta}(\mathbf{k}) \delta(\epsilon_{n\mathbf{k}} - \epsilon_F), \quad (5)$$

with ϵ_F being the Fermi energy. We used an energy cutoff of 320 eV and an $18 \times 18 \times 12$ ($18 \times 18 \times 18$) mesh for the calculation of the optical properties of the BP (rhombic) structure.

The calculated plasma frequencies are reported and compared with the experiment in Fig. 4(e). Although the qualitative behavior is well reproduced, the results consistently overestimate the experimental values by a factor of 3. The onset of the Lifshitz transition is theoretically predicted at 2.1 GPa, close to, but slightly higher than, the 1.5 GPa experimental value. This small discrepancy is likely due to defects and to the anomalous temperature dependence of the band structure [14,37].

Above 3 GPa the theoretical plasma frequency calculated within the A17 structural phase increases linearly with pressure up to 8.5 GPa as experimentally observed [Fig. 4(e)]. Considering the structural phase transition in the A7 phase, we found that the theoretical plasma frequencies [green triangles in Fig. 4(e)] are significantly enhanced with respect to the A17 case. Interestingly, the experimental values can match this leap if one considers the $\omega_{p, \text{Drude+MIR}}$ plasma frequency [green circles in Fig. 4(e)] instead of ω_p . The qualitative agreement between experimental data and theoretical calculations within this large pressure range and in different structural phases indicates that the midinfrared band can be attributed to partially localized charge carriers emerging in the A7 phase and coalescing in a Drude term at higher pressures. This spectral feature, likely related to strong interactions, is intriguing and deserves further study.

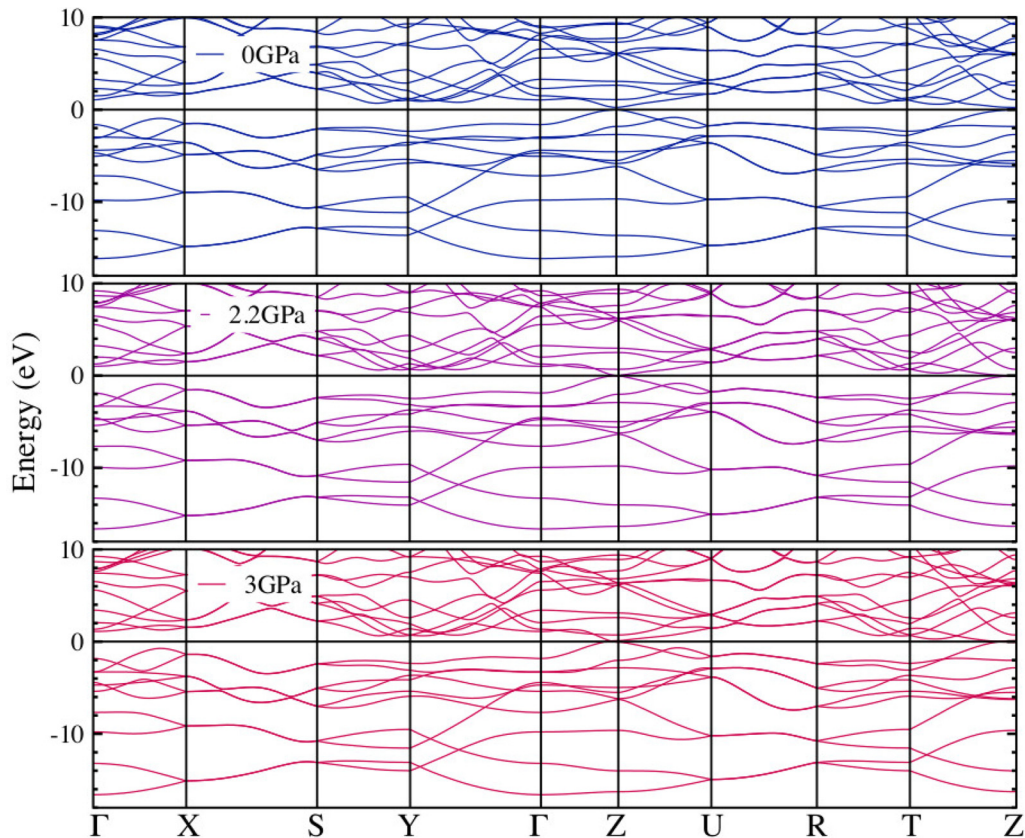


FIG. 5. Band structure calculations at ambient pressure and at 2.2 and 3 GPa. According to the DFT calculations the Lifshitz transition is expected to take place at 2.2 GPa, a slightly larger pressure value with respect to the experimental $P_L = 1.5$ GPa (see main text),

The calculations of the pressure-dependent B_{1u} phonon frequency in Fig. 3(b) have been performed [38] at the relaxed structural positions within the GGA-PBE approximation for the xc correlation DFT functional [39]. The calculations confirm that the observed peak at 130 cm^{-1} , measured in the low-pressure region, originates from an IR active B_{1u} mode of BP, which we were able to follow with pressure. In particular, we calculated that this active phonon mode consists of an out-of-plane oscillation of P dimers in the armchair direction (while the motion is in phase along the zigzag one). Starting at about 133 cm^{-1} at $P = 0$, the phonon shows a negative Grüneisen parameter and softens with pressure, reaching 100 cm^{-1} at 100 GPa. The theoretical redshift is in reasonably good agreement with the experiment. A minor disagreement in the slope is acceptable within the accuracy of the theoretical methods, in particular with respect to the intrinsic error of existing DFT functionals.

VI. CONCLUSIONS

In conclusion, we have presented direct optical identification of a pressure-induced Lifshitz transition in elemental BP ($P_L = 1.5$ GPa). The key spectral feature associated with this transition is a discontinuity in the pressure-dependent carrier density that can be attributed to the emergence of a plasma of massless Dirac carriers. The character of the Lifshitz transition has been confirmed through comparison with DFT calculations that provided an excellent description

of the experimental plasma frequencies. The Dirac plasma frequency increases linearly with pressure, well into the A17-A7 mixed phase up to about 8 GPa. The onset of the A7 structural phase triggers the delocalization of a significant portion of charge carriers, which become indistinguishable from the Dirac carriers when entering into the sc phase above 9 GPa. Our work in a clean, controlled elemental system will serve as a useful guide to identify optical signatures of a Lifshitz transition in more complicated systems, like hole-doped cuprates and iron pnictides, and will lead to a deeper understanding of this fascinating physical phenomenon.

ACKNOWLEDGMENTS

The authors wish to thank A. Cavalleri for providing the DAC for lower pressure measurements, and L. Ortenzi and E. Cappelluti for preliminary discussions on the experimental data. B.J. acknowledges support via the IISc-ICTP fellowship from IISc Bangalore and ICTP Trieste. N.E. and A.G. acknowledge the ERC Grant No. 648589 “SUPER-2D”, funding from DFG projects CRC 1238 (project A1) and GR 3708/2-1.

APPENDIX: DRUDE-LORENTZ FITS TO THE OPTICAL PROPERTIES

The optical conductivity data, as extracted from the Kramers-Kronig transformation of the reflectivity, have been fit to a phenomenological Lorentz-Drude model. One harmonic oscillator is used to fit the phonon mode at the lowest

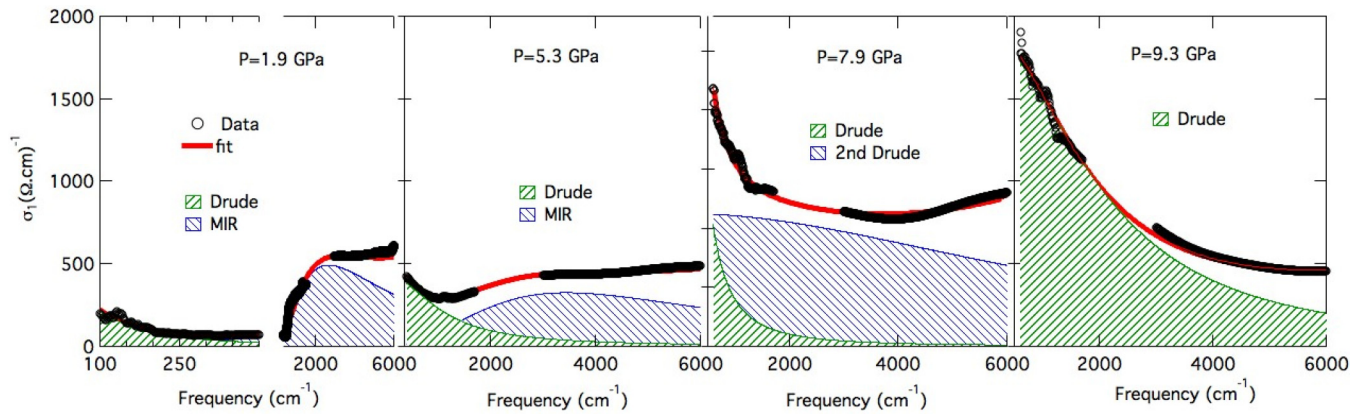


FIG. 6. Pressure dependence of the two Drude-Lorentz fitting components describing the experimental data in the mid- and far-infrared range.

pressures, while a minimum set of three harmonic oscillators (or Drude terms) can be employed in order to reproduce the electronic response. One high-energy harmonic oscillator centered at about $40\,000\text{ cm}^{-1}$, according to band structure calculations [40], is used to capture the electronic contribution from ultraviolet interband absorptions.

The evolution of the two remaining infrared components is shown in Fig. 6 for selected pressures. Between 0.3 and

5.3 GPa, we use just one Drude term and one midinfrared (MIR) band to account for the infrared absorption. With increasing pressure, the two components start overlapping, while the MIR band softens. From 7 to 7.9 GPa, the MIR band evolves in a second Drude term with a scattering rate much larger than the one associated with the first Drude absorption. At 9.3 GPa one single Drude term can be employed to reproduce the experimental infrared data.

- [1] I. M. Lifshitz, *Sov. Phys. JETP* **11**, 1130 (1960).
- [2] M. R. Norman, J. Lin, and A. J. Millis, *Phys. Rev. B* **81**, 180513(R) (2010).
- [3] S. Benhabib, A. Sacuto, M. Civelli, I. Paul, M. Cazayous, Y. Gallais, M. A. Measson, R. D. Zhong, J. Schneeloch, G. D. Gu, D. Colson, and A. Forget, *Phys. Rev. Lett.* **114**, 147001 (2015).
- [4] C. Liu, T. Kondo, R. M. Fernandes, A. D. Palczewski, E. D. Mun, N. Ni, A. N. Thaler, A. Bostwick, E. Rotenberg, J. Schmalian, S. Bud'ko, P. C. Canfield, and A. Kaminski, *Nat. Phys.* **6**, 419 (2010).
- [5] G. E. Volovik, *Phys.-Usp.* **61**, 89 (2018).
- [6] J. Kim, S. S. Baik, S. H. Ryu, Y. Sohn, S. Park, B.-G. Park, J. Delinger, Y. Yi, H. J. Choi, and K. S. Kim, *Science* **349**, 723 (2015).
- [7] N. Ehlen, A. Sanna, B. V. Senkovskiy, L. Petaccia, A. V. Fedorov, G. Profeta, and A. Grüneis, *Phys. Rev. B* **97**, 045143 (2018).
- [8] Q. Liu, X. Zhang, L. B. Abdalla, A. Fazzio, and A. Zunger, *Nano Lett.* **15**, 1222 (2015).
- [9] Z. J. Xiang, G. J. Ye, C. Shang, B. Lei, N. Z. Wang, K. S. Yang, D. Y. Liu, F. B. Meng, X. G. Luo, L. J. Zou, Z. Sun, Y. Zhang, and X. H. Chen, *Phys. Rev. Lett.* **115**, 186403 (2015).
- [10] C.-H. Li, Y.-J. Long, L.-X. Zhao, L. Shan, Z.-A. Ren, J.-Z. Zhao, H.-M. Weng, X. Dai, Z. Fang, C. Ren, and G.-F. Chen, *Phys. Rev. B* **95**, 125417 (2017).
- [11] J. Qiao, X. Kong, Z.-X. Hu, F. Yang, and W. Ji, *Nat. Commun.* **5**, 4475 (2014).
- [12] T. Low, A. S. Rodin, A. Carvalho, Y. Jiang, H. Wang, F. Xia, and A. H. Castro Neto, *Phys. Rev. B* **90**, 075434 (2014).
- [13] R. Fei, V. Tran, and L. Yang, *Phys. Rev. B* **91**, 195319 (2015).
- [14] N. Ehlen, B. V. Senkovskiy, A. V. Fedorov, A. Perucchi, P. Di Pietro, A. Sanna, G. Profeta, L. Petaccia, and A. Grüneis, *Phys. Rev. B* **94**, 245410 (2016).
- [15] P.-L. Gong, D.-Y. Liu, K.-S. Yang, Z.-J. Xiang, X.-H. Chen, Z. Zeng, S.-Q. Shen, and L.-J. Zou, *Phys. Rev. B* **93**, 195434 (2016).
- [16] J. C. Jamieson, *Science* **139**, 1291 (1963).
- [17] T. Kikegawa and H. Iwasaki, *Acta Crystallogr. B* **39**, 158 (1983).
- [18] T. Akai, S. Endo, Y. Akahama, K. Koto, and Y. Maruyama, *High Press. Res.* **1**, 115 (1989).
- [19] D. Sclta, A. Baldassarre, M. Serrano-Ruiz, K. Dziubek, A. B. Cairns, M. Peruzzini, R. Bini, and M. Ceppatelli, *Angew. Chem. Int. Ed.* **56**, 14135 (2017).
- [20] H. Kawamura, I. Shirota, and K. Tachikawa, *Solid State Commun.* **54**, 775 (1985).
- [21] R. Zhang, J. Waters, A. K. Geim, and I. V. Grigorieva, *Nat. Commun.* **8**, 15036 (2017).
- [22] S. Lupi, A. Nucara, A. Perucchi, P. Calvani, M. Ortolani, L. Quaroni, and M. Kiskinova, *J. Opt. Soc. Am. B* **24**, 959 (2007).
- [23] H. K. Mao and P. M. Bell, *J. Geophys. Res.* **91**, 4673 (1986).
- [24] M. Dressel and G. Grüner, *Electrodynamics of Solids: Optical Properties of Electrons in Matter* (Cambridge University Press, Cambridge, 2002).
- [25] A. Perucchi, L. Baldassarre, P. Postorino, and S. Lupi, *J. Phys.: Condens. Matter* **21**, 323202 (2009).
- [26] S. Das Sarma and E. H. Hwang, *Phys. Rev. Lett.* **102**, 206412 (2009).

- [27] Y. Jiang, R. Roldán, F. Guinea, and T. Low, *Phys. Rev. B* **92**, 085408 (2015).
- [28] K. Akiba, A. Miyake, Y. Akahama, K. Matsubayashi, Y. Uwatoko, and M. Tokunaga, *Phys. Rev. B* **95**, 115126 (2017).
- [29] S. Sugai and I. Shirovani, *Solid State Commun.* **53**, 753 (1985).
- [30] J. Guo, H. Wang, F. von Rohr, W. Yi, Y. Zhou, Z. Wang, S. Cai, S. Zhang, X. Li, Y. Li, J. Liu, K. Yang, A. Li, S. Jiang, Q. Wu, T. Xiang, R. J. Cava, and L. Sun, *Phys. Rev. B* **96**, 224513 (2017).
- [31] S. N. Gupta, A. Singh, K. Pal, B. Chakraborti, D. V. S. Muthu, U. V. Waghmare, and A. K. Sood, *Phys. Rev. B* **96**, 094104 (2017).
- [32] B. Joseph, S. Caramazza, F. Capitani, T. Clarté, F. Ripanti, P. Lotti, A. Lausi, D. Di Castro, P. Postorino, and P. Dore, [arXiv:1706.03706](https://arxiv.org/abs/1706.03706).
- [33] J. A. Flores-Livas, A. Sanna, A. P. Drozdov, L. Boeri, G. Profeta, M. Eremets, and S. Goedecker, *Phys. Rev. Mater.* **1**, 024802 (2017).
- [34] F. Tran and P. Blaha, *Phys. Rev. Lett.* **102**, 226401 (2009).
- [35] G. Kresse and J. Furthmüller, *Comput. Mater. Sci.* **6**, 15 (1996).
- [36] M. Gajdoš, K. Hummer, G. Kresse, J. Furthmüller, and F. Bechstedt, *Phys. Rev. B* **73**, 045112 (2006).
- [37] C. E. P. Villegas, A. R. Rocha, and A. Marini, *Nano Lett.* **16**, 5095 (2016).
- [38] P. Giannozzi *et al.*, *J. Phys.: Condens. Matter* **29**, 465901 (2017).
- [39] J. P. Perdew, K. Burke, and M. Ernzerhof, *Phys. Rev. Lett.* **77**, 3865 (1996).
- [40] H. Asahina, Y. Maruyama, and A. Morita, *Physica B+C* **117-118**, 419 (1983).